

RESEARCH ARTICLE | JULY 08 2022

# Space squeezing optics: Performance limits and implementation at microwave frequencies

SCI F

Special Collection: 2022 Future Luminary Collection

Michal Mrnka  ; Euan Hendry; Jaroslav Láćík; Rachel A. Lennon; Lauren E. Barr; Ian Hooper; David B. Phillips

APL Photonics 7, 076105 (2022)

<https://doi.org/10.1063/5.0095735>

## Articles You May Be Interested In

Spaceplate testing shows great promise for miniaturization of optical systems

Scilight (July 2022)

Engineering the carrier lifetime and switching speed in Si-based mm-wave photomodulators

J. Appl. Phys. (December 2022)

Spoof plasmonic Brewster angle transmission for broadband electromagnetic energy squeezing in the microwave regime

J. Appl. Phys. (July 2020)

# Space squeezing optics: Performance limits and implementation at microwave frequencies

SCI F

Cite as: APL Photon. 7, 076105 (2022); doi: 10.1063/5.0095735

Submitted: 12 April 2022 • Accepted: 19 June 2022 •

Published Online: 8 July 2022



View Online



Export Citation



CrossMark

Michal Mrnka,<sup>1,a)</sup> Euan Hendry,<sup>1</sup> Jaroslav Láćík,<sup>2</sup> Rachel A. Lennon,<sup>1</sup> Lauren E. Barr,<sup>1</sup> Ian Hooper,<sup>1</sup> and David B. Phillips<sup>1</sup>

## AFFILIATIONS

<sup>1</sup> School of Physics and Astronomy, University of Exeter, Exeter EX4 4QL, United Kingdom

<sup>2</sup> Department of Radio Electronics, Brno University of Technology, 616 00 Brno, Czech Republic

<sup>a)</sup> Author to whom correspondence should be addressed: M.Mrnka@exeter.ac.uk

## ABSTRACT

Optical systems often largely consist of empty space as diffraction effects that occur through free-space propagation can be crucial for their function. Contracting these voids offers a path to the miniaturization of a wide range of optical devices. Recently, a new optical element—coined “spaceplate”—has been proposed, which is capable of emulating the effects of diffraction over a specified propagation distance using a thinner non-local metamaterial [Reshef *et al.*, Nat. Commun. **12**, 3512 (2021)]. The compression factor of such an element is given by the ratio of the length of free-space that is replaced to the thickness of the spaceplate itself. In this work, we test a prototype spaceplate in the microwave spectral region (20–23 GHz)—the first such demonstration designed to operate in ambient air. Our device consists of a Fabry-Pérot cavity formed from two reflective metasurfaces with a compression factor that can be tuned by varying the size of perforations within each layer. Using a pair of directive horn antennas, we measure a space compression factor of up to ~6 over a numerical aperture (NA) of 0.34 and a fractional bandwidth of 6%. We also investigate the fundamental trade-offs that exist between the compression factor, transmission efficiency, NA, and bandwidth of this single resonator spaceplate design and highlight that it can reach arbitrarily high compression factors by restricting its NA and bandwidth.

© 2022 Author(s). All article content, except where otherwise noted, is licensed under a Creative Commons Attribution (CC BY) license (<http://creativecommons.org/licenses/by/4.0/>). <https://doi.org/10.1063/5.0095735>

24 March 2025 20:46:01

## INTRODUCTION

Free-space optical devices implicitly rely on the redistribution of energy that occurs when light diffracts through empty space. For example, lenses, gratings, and prisms typically modify an incident wavefront at an interface (or pair of closely spaced interfaces). Yet, the desired effect of this modification only becomes apparent once the optical field has propagated some distance beyond the interface, e.g., by focusing a beam or separating it into distinct diffraction orders. This requirement for free-space propagation places limits on the minimum operational volume of a wide range of optical elements and devices, such as cameras, microscopes, telescopes, and spectrometers. The issue of size becomes even more prominent at longer wavelengths in so-called quasi-optical systems common to the terahertz,<sup>1,2</sup> millimetre-wave,<sup>3</sup> and microwave domains.<sup>4</sup> In this regime, free-space diffraction is fundamental for the operation of

antennas<sup>5–8</sup> and beam waveguides,<sup>9</sup> and this can lead to very large optical systems.<sup>10</sup>

Recently, Reshef *et al.*<sup>11</sup> and Guo *et al.*<sup>12</sup> introduced the intriguing new concept of a “spaceplate”—an optical element capable of mimicking the effects of free-space propagation. Crucially, a spaceplate’s thickness ( $d_{\text{SP}}$ ) is thinner than the free-space distance it replaces ( $d_{\text{eff}}$ ); thus, it can potentially be used to contract the volume of optical systems, as shown schematically in Fig. 1. The degree to which space is contracted is captured by the compression factor,  $\mathcal{C}$ , given by the ratio of the emulated free-space propagation distance to the thickness of the spaceplate itself:  $\mathcal{C} = d_{\text{eff}}/d_{\text{SP}}$ .

The effect of free-space propagation over a distance  $d_{\text{eff}}$  may be understood by decomposing an incident monochromatic optical field of wavelength  $\lambda$  into its component plane waves (i.e., spatial Fourier components). These plane waves do not couple to one another during propagation, but each accumulates an

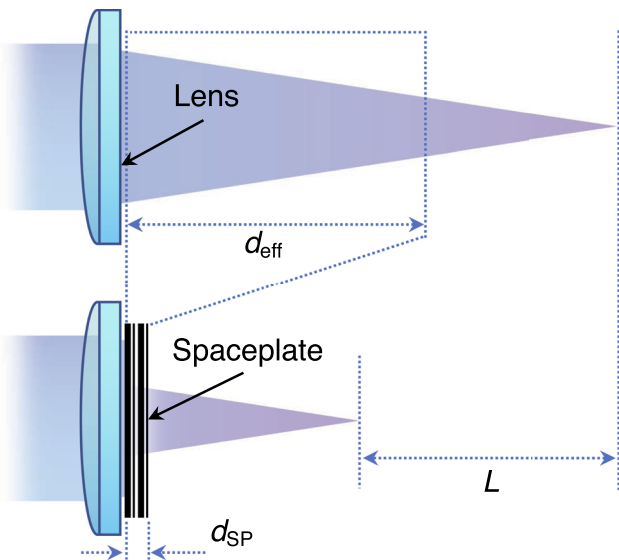


**FIG. 1.** The action of a spaceplate: replacement of a volume of free-space of length  $d_{\text{eff}}$  with an optical element of thickness  $d_{\text{SP}}$ . In this example, a spaceplate is shown in conjunction with a lens to move the focus closer without changing the numerical aperture. The amount of space contracted is  $L = d_{\text{eff}} - d_{\text{SP}}$ .

angle-dependent phase shift of  $\phi = k_z d_{\text{eff}}$ . Here, the wave-vector  $\mathbf{k} = [k_x, k_y, k_z]$  describes the direction each plane wave is travelling in Cartesian coordinates, and  $k_z = k \cos \theta$ , where wavenumber  $k = 2\pi/\lambda = |\mathbf{k}|$  and  $\theta$  is the polar angle of a plane wave with respect to the optical axis. Therefore, in order to emulate free-space propagation, the action of a spaceplate must be “non-local,”<sup>13,14</sup> i.e., it must independently act on the spatial Fourier components of the incident field, imparting an incident angle-dependent phase shift of

$$\phi_{\text{SP}}(\theta) = kd_{\text{eff}} \cos \theta. \quad (1)$$

Designs fall into two main categories, which we term as *stochastic* and *deterministic* spaceplates. Stochastic spaceplates, first introduced in Ref. 11, are non-local metamaterials consisting of a multi-layer stack of homogeneous and isotropic layers distributed along the optical axis. Structuring in 1D in this way ensures that there is no coupling between plane waves incident at different angles, as required. The parameters of individual layers—the thicknesses and refractive indices—can be algorithmically optimized to approximate a spaceplate with a target set of performance characteristics within certain constraints (see Sec. 5 of the [supplementary material](#)).

Deterministic spaceplates are founded on the understanding that certain families of structure readily act as space compressing optics. For instance, the authors of Ref. 11 demonstrated that this is the case for a slab of material of a lower refractive index than the surrounding medium. Guo *et al.* showed that the dispersion associated with a photonic crystal slab can be engineered so that the transmitted field components are imparted non-local phase shifts to mimic free-space propagation.<sup>12,15</sup> Chen and Monticone, meanwhile, highlighted that the angular dispersion in a Fabry-Pérot cavity operating slightly off resonance imparts close to the necessary angle-dependent phase shifts to transmitted light.<sup>16</sup>

However, understanding the limitations on achievable space-plate performance is an open problem. Of the different structures that have been theoretically shown to operate as spaceplates,<sup>11,12,15–17</sup> all exhibit some degree of trade-off between the key parameters defining performance: the *compression factor*; the *transmission efficiency* as a function of incident angle; the *numerical aperture (NA)* and *bandwidth ( $\delta\omega$ )* over which the spaceplate operates; and the total *space contraction length (L)*—see Fig. 1. For example, in all devices proposed so far, prioritizing a high compression factor tends to reduce the achievable NA and bandwidth.<sup>17</sup> Furthermore, as the concept of space-compression optics is relatively new, the only experimental demonstration of a spaceplate to date relied on artificially increasing the refractive index of the ambient environment and demonstrated a relatively modest compression factor of  $\mathcal{C} \sim 1.2$  over the visible spectrum.<sup>11</sup> As such, it is not clear what maximum spatial compression is practically feasible in an air environment, where most envisioned applications lie.

In this work, we design and experimentally test a prototype deterministic spaceplate operating in ambient air in the microwave region (20–23 GHz). Our design consists of a two-layered resonator based on perforated conductive metasurfaces, which form a Fabry-Pérot cavity. We study the performance limits of single resonator-based spaceplates and show that arbitrarily high compression factors may be reached by tuning the reflectance of the cavity mirrors. Experimentally, we demonstrate a spaceplate with a peak compression factor of  $\mathcal{C} = 6$ . We discuss the advantages and drawbacks associated with our proof-of-principle prototype and describe future improvements, which merge the concepts of the deterministic and stochastic spaceplate design. While our focus here is on microwave frequency devices, the scale invariance of Maxwell's equations means that our work is also of relevance to other parts of the electromagnetic spectrum.

## SPACE-COMPRESSION USING A FABRY-PÉROT CAVITY

Resonance features play a significant role in all ambient-air spaceplate designs proposed so far. Therefore, following Ref. 16, we examine the potential of a single Fabry-Pérot cavity, operating slightly off-resonance, to act as a spaceplate. We consider a cavity composed of two semi-transparent mirrors with equal reflectance  $R$ , separated by a distance  $d_{\text{SP}}$ , which corresponds to the thickness of the spaceplate [see Fig. 2(c)]. The complex transmission coefficient, as a function of plane wave incident angle  $\theta$  and angular frequency  $\omega$ , is the sum of the transmitted field components after successive passes around the cavity, which converges to

$$t(\theta, \omega) = \frac{t_1 t_2 \exp(i\beta)}{1 + r_1 r_2 \exp(2i\beta)}, \quad (2)$$

where

$$\beta = \frac{\omega}{c} d_{\text{SP}} \cos \theta. \quad (3)$$

Here,  $t_i$  and  $r_i$  are the fraction of the amplitude of the incident wave transmitted or reflected at mirror  $i$ , respectively. For a single cavity in air, the Stokes relations connect transmission and reflection according to  $r_1 = -r_2$ ,  $r_1^2 = r_2^2 = r^2$ , and  $t_1 t_2 = 1 - r^2$ , assuming absorption is negligible.

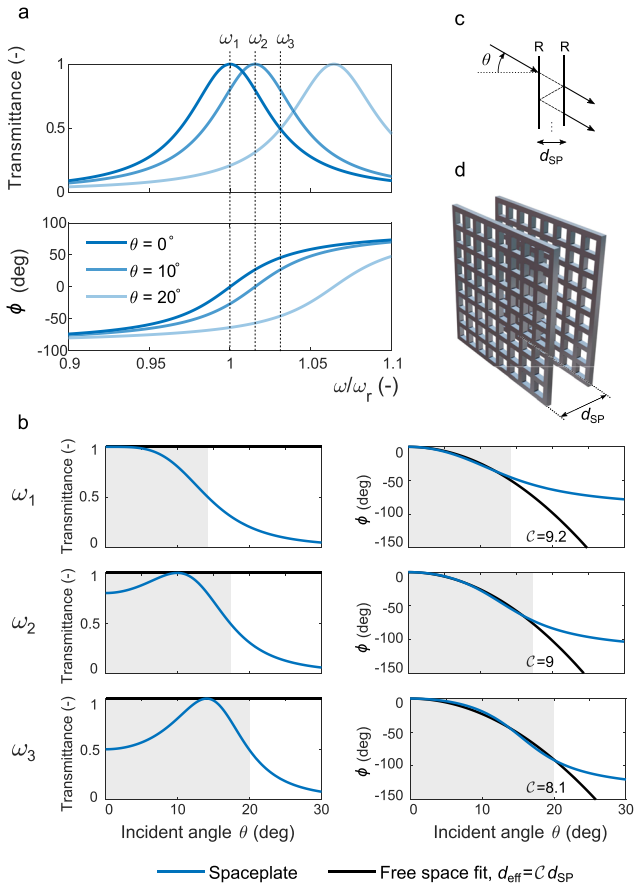


**FIG. 2.** The operation of a Fabry-Pérot cavity-based spaceplate. In this example,  $R \sim 0.8$  and  $d_{\text{SP}} = 7.1$  mm, resulting in a first-order resonance at  $\omega_r \sim 1.3 \times 10^{11}$  rad/s (21 GHz). (a) The resonance line of a Fabry-Pérot cavity shifts approximately quadratically with incidence angle. (b) The transmittance (left column) and phase (right column) as a function of incident angle for three different angular frequencies near resonance ( $\omega_1$ ,  $\omega_2$ , and  $\omega_3$ ). The maximum NA is achieved when the working angular frequency corresponds to  $\omega_3 = \omega_r + \Delta\omega/2$ , where  $\omega_r$  and  $\Delta\omega$  are the resonance frequency and the half power line width. While this maximizes the NA, it also introduces a 50% reflective loss at normal incidence. Higher transmittance at normal incidence can be achieved if the angular frequency is closer to the resonance (e.g.,  $\omega_2$ ). The maximum transmittance and the lowest NA are achieved for  $\omega_1 = \omega_r$ . (c) Schematic view of a general FP cavity formed by mirrors with equal reflectances  $R$ . (d) Schematic view of the spaceplate proposed in this paper—the FP cavity is formed by two perforated conductive sheets acting as mirrors with tunable reflectance.

Within a limited angular range, the resonance frequency of a Fabry-Pérot cavity shifts approximately quadratically as a function of incidence angle—see Sec. 1 of the [supplementary material](#) for more details. This results in a phase shift in the transmitted field that also quadratically depends on the incident angle. [Figure 2\(a\)](#) shows the frequency of the resonance at three different incident angles. [Figure 2\(b\)](#) shows the behavior of the transmitted intensity  $|t|^2$  and phase  $\phi = \arg(t)$  as a function of incident angle for three different frequencies located near to resonance. We can see that, as observed in Ref. 16, within a finite numerical aperture (shaded in gray), the phase change as a

function of the incidence angle mimics that of free-space propagation over a distance  $d_{\text{eff}}$  that is larger than the spaceplate thickness  $d_{\text{SP}}$  (in this case yielding a compression factor of  $\mathcal{C} = d_{\text{eff}}/d_{\text{SP}} \sim 8 - 9$  that is weakly dependent on frequency). The transmitted intensity is  $>50\%$  over this angular range although evidently transmission does vary as a function of incident angle. The largest operating NA occurs when the illumination frequency is slightly higher than the resonance frequency at normal incidence.

Assuming high reflectance (so that  $1 - R \ll 1$ ), the compression factor  $\mathcal{C}$  is related to the quality factor of the resonance ( $Q$ ) and, thus, the reflectance  $R$  of the cavity mirrors,

$$\mathcal{C} = \frac{d_{\text{eff}}}{d_{\text{SP}}} \approx \frac{Q}{2\ell} \approx -\frac{\pi}{2 \ln R}, \quad (4)$$

where  $\ell$  is the order of the resonance (see Sec. 1.3 of the [supplementary material](#) for derivation). Equation (4) demonstrates that arbitrarily high compression factors may be reached by tuning the reflectance  $R$  of the cavity mirrors alone in a manner that is independent of  $\ell$ . For example, a compression factor of  $\mathcal{C} \sim 3200$  can be reached by restricting the angular operating range to  $1^\circ$ . We note that this is a factor of  $\sim 10$  larger than the compression factor of  $\mathcal{C} \sim 340$  recently found by stochastic optimization for an equivalent NA<sup>17</sup>—a design also sharing a similar amplitude modulation function to a Fabry-Pérot-based spaceplate. By further restricting the angular operating range of a Fabry-Pérot cavity to  $0.5^\circ$ , a compression factor of  $\mathcal{C} \sim 13\,000$  can be obtained. We note that this result is consistent with the analysis in Ref. 16.

In Refs. 12 and 16, the authors studied the trade-off between the compression factor and NA in resonator-based spaceplate designs. Here, for the first time, we include the role of spectral bandwidth while also stipulating the minimum transmission efficiency. The interplay between these parameters can be encapsulated in a simple relation linking the NA to  $\mathcal{C}$  and the desired operating bandwidth  $\delta\omega$ , found by considering the Q-factor of the resonance (see Sec. 1.4 of the [supplementary material](#)),

$$\text{NA} \sim [1 - [1 + 1/(2\mathcal{C}\ell) - \delta\omega/\omega_r]^{-2}]^{\frac{1}{2}}, \quad (5)$$

where  $\omega_r$  is the angular frequency of the resonance. In deriving Eq. (5), we define the useable NA as the region over which the spaceplate transmits  $>50\%$  of incident power, while the desired bandwidth and compression factor must also satisfy  $\delta\omega \leq \omega_r/(2\mathcal{C}\ell)$  to ensure the operational frequency range remains close to a resonance. In this analysis, we have assumed that  $R$  is nominally independent of frequency and incident angle. Rearranging Eq. (5) for the fractional bandwidth  $\delta\omega/\omega_r$  yields the following:

$$\delta\omega/\omega_r \sim 1 + (2\mathcal{C}\ell)^{-1} - (1 - \text{NA}^2)^{-\frac{1}{2}}, \quad (6)$$

where here the choice of NA and compression factor must satisfy the condition

$$\text{NA}^2 \leq 1 - (1 + (2\mathcal{C}\ell)^{-1})^{-2} \quad (7)$$

to ensure that the linewidth of the resonator is wide enough to accommodate the target compression factor over the specified NA.

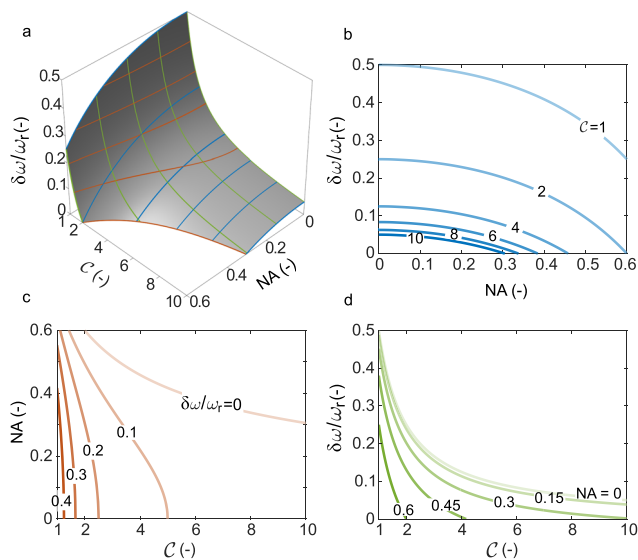


**FIG. 3.** Performance limits of Fabry-Pérot-based spaceplates. (a)–(d) Allowed combinations of compression factor, NA, and fractional bandwidth, constrained by ensuring the transmission efficiency of >50%.

Equations (5)–(7) demonstrate the key trade-offs inherent in all spaceplate designs: higher compression factors are obtained at the expense of a reduced NA and bandwidth. Figure 3 illustrates these trade-offs, which will profoundly impact the applicability of high-compression spaceplates. See Sec. 1.4 of the [supplementary material](#) for more details.

## EXPERIMENTAL DEMONSTRATION OF A SPACEPLATE

An important step is to explore the extent to which space-compression is readily achievable under experimental conditions. To investigate this, we have built a spaceplate based on two reflective metasurfaces, which form a Fabry-Pérot cavity. Our prototype is designed to operate with a compression factor of up to  $C \sim 6$  over an NA of  $\sim 0.34$  in air (i.e., a maximum incident angle  $\sim 20^\circ$ ) and a frequency range of 20.8–22.1 GHz. We note that although the optical properties of Fabry-Pérot cavities are well-understood, here, we experimentally study them from the novel perspective of space-compression.

The partially reflecting cavity mirrors are implemented with a simple metamaterial: a conductive sheet perforated with sub-wavelength sized square holes, as depicted in Fig. 2(d). These perforated layers must not couple the spatial Fourier components of transmitted radiation—a constraint satisfied when the wavelength of radiation is larger than the period of the structure. Under this condition, the perforated metal behaves as homogeneous layer: a conductor with an effective plasma frequency considerably lower than the constituent metal.<sup>18</sup> The effective, frequency-dependent permittivity of the layer is determined by the size and spacing of holes, allowing for the creation of mirrors with well-controlled and near-arbitrary reflectivity. See Sec. 2 of the [supplementary material](#) for more details of this metasurface-based mirror design. Here, we choose

the geometry of the perforations to yield a reflectance of  $R \sim 0.8$ . The cavity consists of two metasurfaces, each of area  $0.3 \times 0.3$  m<sup>2</sup> separated to give an overall spaceplate thickness of  $d_{SP} \sim 9.6$  mm. In this case, the first order ( $\ell = 1$ ) Fabry-Pérot resonance occurs at 21 GHz (see Sec. 3.2 of the [supplementary material](#)).

We first measure the dispersion of our prototype spaceplate, which is shown in Fig. 4. The spaceplate is illuminated with a source approximating a plane wave using a horn antenna, and the intensity and corresponding phase shift of the transmitted field are measured with a second horn antenna. Measurements are made as a function of polarization, frequency, and incident angle—adjusted by rotating the spaceplate with respect to the source and detector, as shown in Fig. 4(a). The data are collected using a vector network analyzer (VNA) and normalized to the system response in the absence of the spaceplate. See Sec. 4 of the [supplementary material](#) for more details of this experiment.

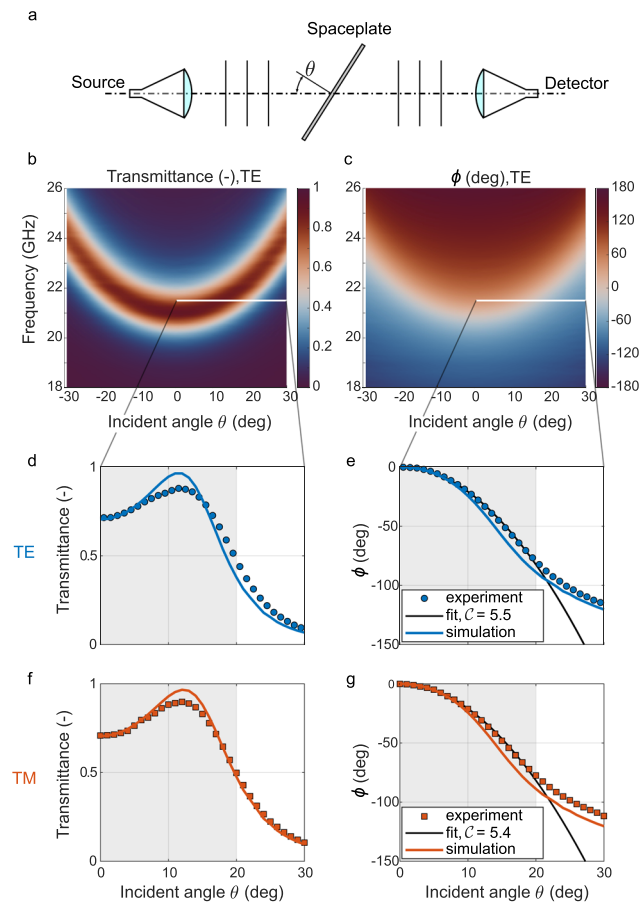


**FIG. 4.** Spaceplate dispersion measurement. (a) Schematic of the experimental setup. (b) Transmittance and (c) phase shift imparted by a spaceplate as a function of incident angle and frequency (TE polarization). (d) and (e) Cross section cuts through the TE dispersion relations. (e) Best fit free-space propagation phase function (black line), corresponding to a compression factor of  $C = 5.5$ . (f) and (g) Cross section cuts through the measured TM dispersion relations (see the [supplementary material](#) for full dispersion plots).

We observe a well-defined resonance band in the dispersion plots for both the TE and TM incident radiation. Figures 4(b) and 4(c) show the TE case; see Sec. 4 of the [supplementary material](#) for the TM measurement. Figures 4(d) and 4(e) show angular cross sections through the dispersion maps at a frequency of 21.5 GHz. We see that the phase shift changes quadratically as a function of incident angle over the NA of the spaceplate (shaded in gray). To extract an estimate of the compression factor, we search for the effective propagation distance  $d_{\text{eff}}$  that has incident-angle-dependent phase-shifts that best fit our measurements. We find that the angular phase-shifts corresponding to a propagation distance of  $d_{\text{eff}} = 53$  mm closely fit to our experimental data [black line in Fig. 4(e)], indicating a compression factor of  $C = d_{\text{eff}}/d_{\text{SP}} = 5.5$ . Figures 4(f) and 4(g) show the equivalent result for TM polarization, yielding  $C = 5.4$ .

We also verify the analytical design of our spaceplate with finite-element simulations incorporating the sub-wavelength scale features of the metasurface mirrors (performed in Ansys High Frequency Simulation Software - HFSS). These simulations also closely match our experimental results, shown as colored lines in Figs. 4(d)-4(g). See Sec. 3 of the [supplementary material](#) for more details of this numerical model.

Repeating this analysis for different illumination frequencies enables calculation of the compression factor  $C(f)$  as a function of illumination frequency  $f$ —signifying the bandwidth of our spaceplate. Figure 5(e) shows the result of this calculation for both

TE and TM polarizations. We observe reasonable agreement with our finite-element model: the slightly lower compression factors measured experimentally are due to the inhomogeneous broadening of the resonance peak compared with that simulated (see [supplementary material](#), Sec. 3, Fig. 11). A secondary effect may be caused by the illumination field only approximating a plane wave and, in reality, containing a small spread of wavevectors. This will also act to slightly reduce the measured Q-factor of the resonance.

When in use, a spaceplate must be able to separately address the spatial Fourier components of an incident wave without causing any coupling between them. While our dispersion measurements demonstrate the key characteristics of space compression when illuminated by individual plane waves, it is also instructive to study our spaceplate's ability to operate on incident radiation containing many Fourier components simultaneously. Therefore, we next study the response of our spaceplate when illuminated by a diverging field and spatially map the transmitted radiation. This enables direct measurement of the change in wavefront curvature when the spaceplate is introduced into the beam-path. In contrast to our dispersion measurements, this will be sensitive to any coupling between Fourier components due to unwanted scattering from defects or the edges of the spaceplate.

Our experiment is shown schematically in Figs. 5(a) and 5(b). We position an antenna approximating a point-source  $\sim 150$  mm behind the spaceplate and measure the transmitted field along a

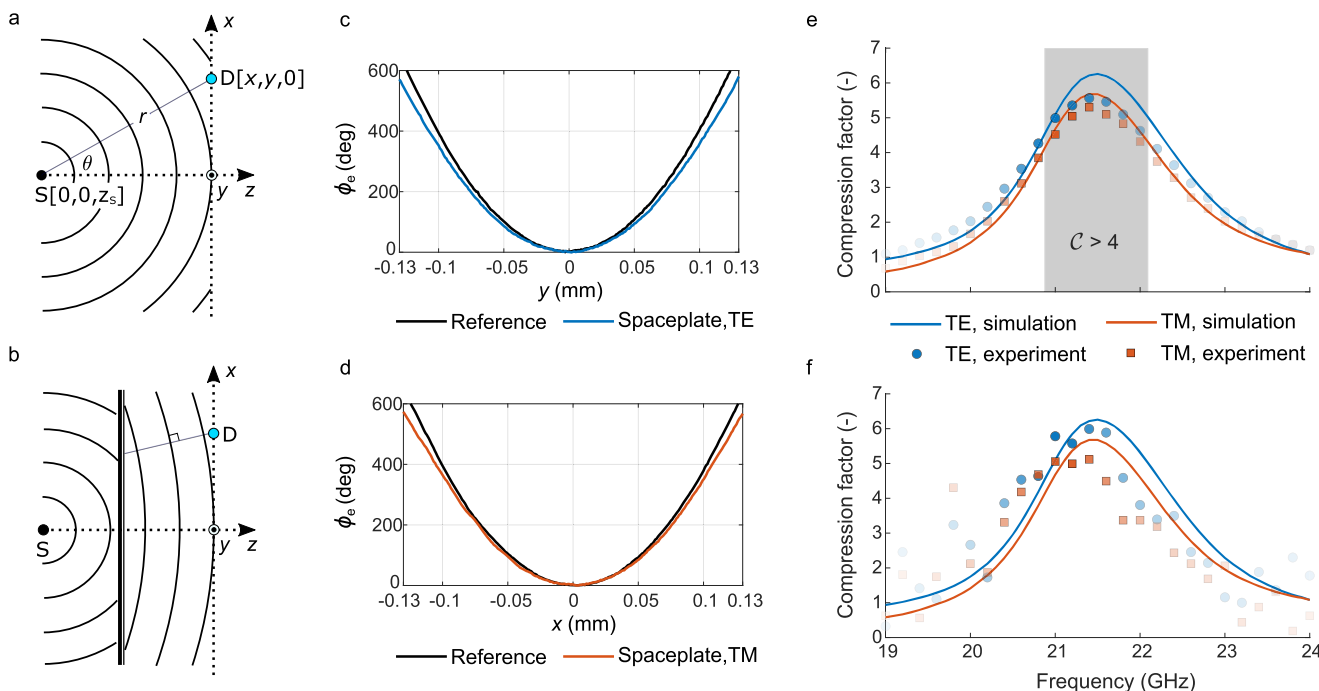


**FIG. 5.** (a) Schematic of the field scan reference measurement. (b) Schematic of the spaceplate field scan measurement. (c) The change in the wavefront curvature when the spaceplate is inserted into the measurement system (TE). (d) Equivalent to (c) but for TM polarization. (e) Compression factor as a function of incident frequency, calculated from the spaceplate dispersion measurement. (f) Compression factor as a function of incident frequency, calculated from the spaceplate field-scan measurement. The transparency of the points in (e) and (f) has been modulated in proportion to the transmitted intensity.

horizontal line-scan, parallel to the plane of the spaceplate  $\sim 150$  mm beyond it. The measured wavefronts, when illuminating with TE and TM polarizations, are shown in Figs. 5(c) and 5(d), without (black line) and with (colored lines) the spaceplate present in the beam-path. As expected, we see that the curvature of the wavefronts decreases when the spaceplate is inserted into the system as the transmitted field emulates that of a field that has propagated further from the point source. The smooth variation in the phase of the field transmitted through the spaceplate indicates that scattering effects are minimal as interference would appear as oscillations.

The frequency-dependent compression factor  $C(f)$  can also be calculated from this measured change in wavefront curvature. At each illumination frequency, we find the apparent distance,  $\delta z$ , from the measurement plane to an ideal point source that has a phase curvature that best fits the measured phase curvature. We carry out this procedure on data with the spaceplate present ( $\delta z_{\text{SP}}$ ) and without the spaceplate in the system ( $\delta z_{\text{ref}}$ ). The length of space contracted is  $L(f) = \delta z_{\text{SP}}(f) - \delta z_{\text{ref}}(f)$ , and the compression factor is, then, inferred via  $C(f) = (L(f) + d_{\text{SP}})/d_{\text{SP}}$  (e.g., see Fig. 1).

Figure 5(f) shows the result of this calculation. Here, the results follow the expected trend although the data are noisier than the frequency-dependent compression factor calculated from the dispersion measurement, and a small systematic shift in the frequency of the peak position is observed in both polarizations. There are two reasons why field-mapping measurements are more subject to error: they are obtained by scanning the position of the detection antenna, which can introduce minor systematic or random phase drifts due to the change in the configuration of the cable, leading to the VNA during the scan. In addition, in this experiment, the emitting antenna only approximates a point source, and so the apparent position of an ideal point source that best fits the data (also known as the “phase center”) can be subject to systematic errors that depend on frequency. In both experiments, we expect the error to be highest in the wings of the curves, where the intensity of the transmitted field is low, and so any errors in phase measurements are magnified in these regions when the compression factor is calculated. To indicate this, we have modulated the transparency of the data points in proportion to the transmitted intensity in the plots. In the region of high transmission, there is an agreement between the compression ratios calculated using both measurement approaches, which indicates that our spaceplate is operating as designed.

## DISCUSSION

All of the spaceplate designs proposed thus far<sup>11,12,15–17</sup> exhibit trade-offs between the achievable compression factor, transmission efficiency, NA, bandwidth, and total space contraction length. Here, we have focused on the simplest deterministic spaceplate design, a single Fabry-Pérot cavity, and highlighted that it can achieve a compression factor of nearly an order-of-magnitude higher than the largest quoted compression factor recently found by stochastic optimization over an equivalent NA.<sup>17</sup>

A single Fabry-Pérot cavity-based spaceplate has two main drawbacks: there is a weak dependence of the compression factor on the incident polarization [see Fig. 5(e)], and transmitted intensity is modulated as a function of both frequency and angle [see

Fig. 2(b)]. However, coupling together a series of Fabry-Pérot cavities provides opportunities to overcome these issues. For example, Chen and Monticone theoretically showed that the transmission efficiency, along with the total space contraction length of a spaceplate, can be enhanced using coupled Fabry-Pérot cavities while trading a modest reduction in the compression factor.<sup>16</sup>

Stochastic optimization schemes also seem to generate spaceplate designs, which are essentially coupled Fabry-Pérot cavities. For example, in order to overcome the limitations of a single Fabry-Pérot cavity, we have explored the use of a genetic algorithm to optimize the layer-spacing of a spaceplate consisting of up to 15 elements. See Sec. 5 of the [supplementary material](#) for the details of our optimization algorithm and results. We give the optimizer freedom to merge and, thus, reduce the number of layers when seeking an optimal solution. Using this method, we find a locally optimal solution consisting of three Fabry-Pérot cavities separated by two optimized ( $\sim \lambda/6$ ) coupling regions, which is very similar to the deterministic design presented by Chen and Monticone.<sup>16</sup> These coupled cavity spaceplate designs are able to suppress the polarization dependence exhibited by a single Fabry-Pérot cavity and generate a roughly constant transmission as a function of incident angle over the operating NA.

Taken together, the apparent dependence of all spaceplate designs on Fabry-Pérot resonance effects suggests that the trade-offs inherent in a single Fabry-Pérot cavity may be close to the fundamental and technical limits on spaceplate performance. We speculate that a Fabry-Pérot cavity may be understood as a basic building block of a spaceplate in the same way as a simple lens is a basic building block of a multi-element (e.g., objective) lens. We envisage that the majority of future spaceplate designs will feature coupled Fabry-Pérot cavities, which will be honed for specific applications—such as the optimization of performance around three distinct color channels for color imaging—in a similar manner to the way compound lenses are designed to suppress the chromatic and Seidel aberrations present in a single lens.

While in the process of updating our manuscript, a second study on the fundamental limits of spaceplates was released, making an elegant link between space compression and slow light research.<sup>19</sup> The bounds derived in this work are close to our analysis, while being marginally less restrictive, and a similar trade-off between the compression factor, bandwidth, and NA is shown. However, we note that while our exploration of spaceplate performance constrains the transmission efficiency to be greater than 50%, the approach in Ref. 19 does not constrain transmission efficiency—one of the key parameters defining spaceplate performance. We would expect an improvement in performance beyond the limits given in Eqs. (5) and (6) might be possible by relaxing constraints on the acceptable level of transmission. As yet there is no concrete strategy to design spaceplates that can outperform Fabry-Pérot cavities, it will be interesting to see if this becomes possible in the future.

It is also worth noting that the ability of a Fabry-Pérot cavity to non-locally modify the angular spectrum of electromagnetic waves is well-known to the antenna and microwave communities. Fabry-Pérot resonator antennas, first proposed by Trentini *et al.* in Ref. 20, increase the directivity of an antenna by coupling it to a Fabry-Pérot resonator with considerably larger lateral dimensions.<sup>21</sup> It is also already understood that wavefronts emanating

from the structure have traveled a longer path length than the thickness of the antenna, as theoretically derived by Burghignoli in Ref. 22, which is consistent with the theoretical behavior of a space-plate. We emphasize that in these earlier studies, the applications in mind were very different from the concept of space-compression.

## CONCLUSIONS

In summary, we have experimentally demonstrated a deterministically tunable space-squeezing optical element in the microwave spectral region. We observe a maximum space compression factor of  $\sim 5.5$  over an NA of 0.34 at 21.5 GHz. The compression factor is higher than 4 in the frequency band of 20.8–22.1 GHz. We believe that this is a significant step toward the introduction of the spaceplate concept into real-world quasi-optical systems. Our study hints a Fabry-Pérot cavity may offer a close-to-optimal trade-off in capabilities, as encompassed by Eq. (5), suggesting that this type of simple spaceplate should be used as a benchmark for evaluating the performance of other designs.

## SUPPLEMENTARY MATERIAL

See the [supplementary material](#) for the derivation of the performance trade-off equations, experimental and numerical methods and results, and an analysis of a stochastically designed spaceplate.

## ACKNOWLEDGMENTS

The authors thank Alex Powell for help with early parts of the project. The authors acknowledge financial support from the Engineering and Physical Sciences Research Council (Grant Nos. EP/R004781/1 and EP/S036466/1). Initial measurements were supported by the Internal Grant Agency of Brno University of Technology (Project No. FEKT-S-20-6526). D.B.P. acknowledges the Royal Academy of Engineering and the European Research Council (Grant No. 804626) for financial support.

## AUTHOR DECLARATIONS

### Conflict of Interest

The authors have no conflicts to disclose.

### Author Contributions

**Michal Mrnka:** Conceptualization (equal); Investigation (lead); Methodology (lead); Validation (equal); Writing – original draft (equal); Writing – review & editing (equal). **Euan Hendry:** Conceptualization (equal); Funding acquisition (equal); Investigation (supporting); Methodology (supporting); Supervision (supporting); Writing – original draft (equal); Writing – review & editing (equal). **Jaroslav Láćik:** Investigation (supporting). **Rachel A. Lennon:** Validation (supporting). **Lauren E. Barr:** Investigation (supporting). **Ian Hooper:** Validation (lead). **David B. Phillips:** Conceptualization (equal); Funding acquisition (equal); Investigation (supporting); Methodology (supporting); Supervision (lead); Writing – original draft (equal); Writing – review & editing (equal).

## DATA AVAILABILITY

The data that support the findings of this study are available from the corresponding author upon reasonable request.

## REFERENCES

- <sup>1</sup>R. I. Stantchev, D. B. Phillips, P. Hobson, S. M. Hornett, M. J. Padgett, and E. Hendry, “Compressed sensing with near-field THz radiation,” *Optica* **4**, 989–992 (2017).
- <sup>2</sup>R. I. Stantchev, X. Yu, T. Blu, and E. Pickwell-MacPherson, “Real-time terahertz imaging with a single-pixel detector,” *Nat. Commun.* **11**, 2535 (2020).
- <sup>3</sup>L. E. Barr, P. Karlsen, S. M. Hornett, I. R. Hooper, M. Mrnka, C. R. Lawrence, D. B. Phillips, and E. Hendry, “Super-resolution imaging for sub-IR frequencies based on total internal reflection,” *Optica* **8**, 88 (2021).
- <sup>4</sup>P. F. Goldsmith, *Quasioptical Systems: Gaussian Beam Quasioptical Propagation and Applications* (Wiley-IEEE Press, 1998).
- <sup>5</sup>S. V. Hum and J. Perruisseau-Carrier, “Reconfigurable reflectarrays and array lenses for dynamic antenna beam control: A review,” *IEEE Trans. Antennas Propag.* **62**, 183–198 (2014).
- <sup>6</sup>M. H. Dahri, M. I. Abbasi, M. H. Jamaluddin, and M. R. Kamarudin, “A review of high gain and high efficiency reflectarrays for 5G communications,” *IEEE Access* **6**, 5973–5985 (2018).
- <sup>7</sup>Y. J. Guo, M. Ansari, R. W. Ziolkowski, and N. J. G. Fonseca, “Quasi-optical multi-beam antenna technologies for 5G and 6G mmWave and THz networks: A review,” *IEEE Open J. Antennas Propag.* **2**, 807–830 (2021).
- <sup>8</sup>B. Imaz-Lueje, D. R. Prado, M. Arrebola, and M. R. Pino, “Reflectarray antennas: A smart solution for new generation satellite mega-constellations in space communications,” *Sci. Rep.* **10**, 21554 (2020).
- <sup>9</sup>J. E. Degenford, M. D. Sirkis, and W. H. Steier, “The reflecting beam waveguide,” *IEEE Trans. Microwave Theory Tech.* **12**, 445–453 (1964).
- <sup>10</sup>C. Cappellini, P. H. Nielsen, R. Appleby, R. Wyld, and E. Saenz, “Detailed design and RF analysis of a scatterometer for material characterization in the 50–750 GHz range,” in *the 12th European Conference on Antennas and Propagation (EuCAP 2018)* (IEEE, 2018), pp. 1–5.
- <sup>11</sup>O. Reshef, M. P. Delmastro, K. K. M. Bearne, A. H. Alhulaymi, L. Giner, R. W. Boyd, and J. S. Lundeen, “An optic to replace space and its application towards ultra-thin imaging systems,” *Nat. Commun.* **12**, 3512 (2021).
- <sup>12</sup>C. Guo, H. Wang, and S. Fan, “Squeeze free space with nonlocal flat optics,” *Optica* **7**, 1133–1138 (2020).
- <sup>13</sup>J. Elser, V. A. Podolskiy, I. Salakhutdinov, and I. Avrutsky, “Nonlocal effects in effective-medium response of nanolayered metamaterials,” *Appl. Phys. Lett.* **90**, 191109 (2007).
- <sup>14</sup>J. R. Capers, S. J. Boyes, A. P. Hibbins, and S. A. R. Horsley, “Designing the collective non-local responses of metasurfaces,” *Commun. Phys.* **4**, 209 (2021).
- <sup>15</sup>O. Y. Long, C. Guo, W. Jin, and S. Fan, “Polarization-independent isotropic nonlocal metasurfaces with wavelength-controlled functionality,” *Phys. Rev. Appl.* **17**, 024029 (2022).
- <sup>16</sup>A. Chen and F. Monticone, “Dielectric nonlocal metasurfaces for fully solid-state ultrathin optical systems,” *ACS Photonics* **8**, 1439–1447 (2021).
- <sup>17</sup>J. T. R. Pagé, O. Reshef, R. W. Boyd, and J. S. Lundeen, “Designing high-performance propagation-compressing spaceplates using thin-film multilayer stacks,” *Opt. Express* **30**, 2197–2205 (2022).
- <sup>18</sup>E. K. Stone and E. Hendry, “Dispersion of spoof surface plasmons in open-ended metallic hole arrays,” *Phys. Rev. B* **84**, 035418 (2011).
- <sup>19</sup>K. Shastri and F. Monticone, “To what extent can space be compressed?,” *Bandwidth Limits of Spaceplates* (published online, 2022).
- <sup>20</sup>G. V. Trentini, “Partially reflecting sheet arrays,” *IRE Trans. Antennas Propag.* **4**, 666–671 (1956).
- <sup>21</sup>Z.-g. Liu, “Fabry-Perot resonator antenna,” *J. Infrared, Millimeter, Terahertz Waves* **31**, 391 (2009).
- <sup>22</sup>P. Burghignoli, “Phase centre of Fabry-Pérot cavity antennas: Leaky-wave model and analytical formulas,” in *2012 6th European Conference on Antennas and Propagation (EUCAP)* (IEEE, 2012).